Monthly Notices of the ROYAL ASTRONOMICAL SOCIETY

MNRAS **486,** 1438–1447 (2019)
Advance Access publication 2019 April 4

doi:10.1093/mnras/stz886

*K*2 Ultracool Dwarfs Survey – V. High superflare rates on rapidly rotating late-M dwarfs

R. R. Paudel,[1★] J. E. Gizis,[1] D. J. Mullan,[1] S. J. Schmidt,[2] A. J. Burgasser,[3] P. K. G. Williams,[4] A. Youngblood[5] and K. G. Stassun[6]

[1]*Department of Physics and Astronomy, University of Delaware, Newark, DE 19716, USA*
[2]*Leibniz-Institute for Astrophysics Potsdam (AIP), An der Sternwarte 16, D-14482 Potsdam, Germany*
[3]*Center for Astrophysics and Space Science, University of California San Diego, La Jolla, CA 92093, USA*
[4]*Harvard-Smithsonian Center for Astrophysics, 60 Garden Street, Cambridge, MA 02138, USA*
[5]*NASA Goddard Space Flight Center, Greenbelt, MD 20771, USA*
[6]*Vanderbilt University, Department of Physics & Astronomy, 6301 Stevenson Center Ln., Nashville, TN 37235, USA*

Accepted 2019 March 22. Received 2019 March 22; in original form 2018 December 18

ABSTRACT

We observed strong superflares (defined as flares with energy in excess of 10^{33} erg) on three late-M dwarfs: 2MASS J08315742+2042213 (hereafter 2M0831+2042; M7 V), 2MASS J08371832+2050349 (hereafter 2M0837+2050; M8 V), and 2MASS J08312608+2244586 (hereafter 2M0831+2244; M9 V). 2M0831+2042 and 2M0837+2050 are members of the young (∼700 Myr) open cluster Praesepe. The strong superflare on 2M0831+2042 has an equivalent duration (ED) of 13.7 h and an estimated energy of 1.3×10^{35} erg. We observed five superflares on 2M0837+2050, on which the strongest superflare has an ED of 46.4 h and an estimated energy of 3.5×10^{35} erg. This energy is larger by 2.7 orders of magnitude than the largest flare observed on the older (7.6 Gyr) planet-hosting M8 dwarf TRAPPIST-1. Furthermore, we also observed five superflares on 2M0831+2244 which is probably a field star. The estimated energy of the strongest superflare on 2M0831+2244 is 6.1×10^{34} erg. 2M0831+2042, 2M0837+2050, and 2M0831+2244 have rotation periods of 0.556 ± 0.002, 0.193 ± 0.000, and 0.292 ± 0.001 d, respectively, which we measured by using *K*2 light curves. We compare the flares of younger targets with those of TRAPPIST-1 and discuss the possible impacts of such flares on planets in the habitable zone of late-M dwarfs.

Key words: stars: activity – stars: flare – stars: individual: (2MASS J08371832+2050349, 2MASS J08315742+2042213, 2MASS J08312608+2244586, TRAPPIST-1) – stars: low-mass.

1 INTRODUCTION

M dwarfs make up ∼75 per cent of all main-sequence stars in the local stellar population and are commonly referred to as red dwarfs (Clements et al. 2017). They are smaller, cooler, and less luminous than the Sun. Using the full 4-yr *Kepler* data, Dressing & Charbonneau (2015) estimated an occurrence rate of $0.24^{+0.18}_{-0.08}$ Earth-size planets and $0.21^{+0.11}_{-0.06}$ super-Earths per M dwarf habitable zone (HZ). These results and the discovery of the TRAPPIST-1 planetary system (Gillon et al. 2016, 2017; Luger et al. 2017) demonstrate that there is a significant chance of finding habitable planets around M dwarfs. The *Transiting Exoplanet Survey Satellite (TESS;* Ricker 2014*)* will find many more HZ planets orbiting M dwarfs (Barclay, Pepper & Quintana 2018). With the discovery of many such planets, an essential next step in exoplanet research is to identify those with maximum probability of being habitable, especially those bright enough to be characterized by upcoming missions such as NASA's *James Webb Space Telescope (JWST)*.

Because the M dwarfs have smaller luminosity L than the Sun, in order to have the right temperature for liquid water to exist, the HZ around them must have average orbital radii R ($\sim L^{0.5}$) that are a fraction of an au. TRAPPIST-1, with $L = 5 \times 10^{-4}$ $L_\odot$ (Van Grootel et al. 2018) has an HZ at 0.022 au, i.e. closer to the parent star by a factor of ∼50 than the Earth is to the Sun. Furthermore, M dwarfs are typically magnetically active, with frequent flares from systems with ages of a few million years to billions of years (Lacy, Moffett & Evans 1976; Davenport 2016; Paudel et al. 2018a). CFHT-BD-Tau 4 is an example of a very young ∼1 Myr old M7 dwarf on which a superflare with energy up to 10^{38} erg, was observed (Paudel et al. 2018b) and TRAPPIST-1 is an example of an old star

★ E-mail: rpaudel@udel.edu

with age 7.6 ± 2.2 Gyr (Burgasser & Mamajek 2017) on which multiple flares were observed (Paudel et al. 2018a). The energy of the strongest flare observed on TRAPPIST-1 was 7.1 × 10^{32} erg in the ultraviolet/visible/infrared wavelengths (Paudel et al. 2018a). SDSS J022116.84+194020.4 (M8 dwarf) is another example of a late-M dwarf, whose estimated age is in between ∼200 Myr and few Gyr, and on which a superflare with a total *U*-band energy of ∼10^{34} erg was observed (Schmidt et al. 2014). The closeness of the HZ to the parent star in an M dwarf planetary system implies that any planets located in the HZ of M dwarfs are more likely to be exposed to enhanced X-rays, UV radiation, high-energy particles, and coronal mass ejections (CMEs) associated with flares on the parent star. For example, if a flare occurs on Proxima Centauri (Prox Cen; M5.5 dwarf) with the same energy as a typical solar flare, then the HZ planet Prox Cen b receives 250× more X-rays than Earth, 30× more extreme ultraviolet (EUV) flux, and 10× more far-ultraviolet (FUV) flux (Ribas et al. 2016). The intense radiation and energetic particles may perturb the thermochemical equilibrium of the planet's atmosphere, including the destruction of ozone layer and loss of surface water.

Segura et al. (2010) and Tilley et al. (2017) have reported on modelling the effects of flares on planetary atmospheres. Segura et al. (2010) studied the possible impacts of the 1985 April 12 flare from the dM3 star AD Leo (Hawley & Pettersen 1991), on an Earth-like planet in the HZ of this mid-M dwarf. Likewise, Tilley et al. (2017) studied the effects of high flare rate and high flare energies ($10^{30.5}$–10^{34} erg) of the dM4 flare star GJ1243 on an Earth-like planet. In general, both studies find that if the flare output consists only of photons, then no significant ozone layer destruction occurs. In order to destroy the ozone, the main contributors must be energetic particles analogous to the solar energetic particles (SEP) which are generated along with coronal mass ejections (CMEs) in large solar flares. Assuming that particle fluxes can be generated by scaling from solar flares, Tilley et al. (2017) calculate that, in the case of a stellar flare with energy 10^{34} ergs, the CME/SEP effects could cause extensive ozone destruction on time-scales of years to decades. Even smaller repeated events can lead to extensive ozone destruction on century-long time-scales (Youngblood et al. 2017). However, studies of Type II radio bursts in flare stars (Crosley & Osten 2018) indicate that a simple scaling from solar CME rates to CMEs in stellar flares is not consistent with their data: they conclude that this 'casts serious doubt on the assumption that a high flaring rate corresponds to a high rate of CMEs'. As a result, impact of flares on ozone layer depletion remains under investigation.

In order to assess the habitability of M dwarf planets, it is important to constrain the flare rates of M dwarfs as a function of their masses and ages. Because of this, we have been studying the flare rates of various mid- and late-M dwarfs and early-L dwarfs which were observed by the *K*2 mission (Howell et al. 2014) in various campaigns (see e.g. Gizis et al. 2017b; Paudel et al. 2018a). Here we present our results on superflares which we have observed on three late-M dwarfs: 2MASS J08315742+2042213 (hereafter 2M0831+2042), 2MASS J08371832+2050349 (here-

Table 1. Properties of targets.

PHOTOMETRIC PROPERTIES

Target name	sp. type	$\tilde{K}_p$ (mag)	*J* (mag)	*K* (mag)	*i* (mag)	H α EW Å
2M0831+2042	M7	19.6	15.56 ± 0.06	14.70 ± 0.09	18.51 ± 0.01	9.3 ± 0.3[a]
2M0837+2050	M8	20.0	15.90 ± 0.07	14.88 ± 0.09	18.80 ± 0.01	20.3 ± 0.6[a]
2M0831+2244	M9	19.8	14.91 ± 0.04	13.84 ± 0.04	18.77 ± 0.01	7.3 ± 0.5[a]
TRAPPIST-1	M8	15.9	11.35 ± 0.02	10.30 ± 0.02	15.11 ± 0.00	4.9[b]

KINEMATIC PROPERTIES

	μ_α (mas yr^{-1})	μ_δ (mas yr^{-1})	$V_{\tan}$ (km s^{-1})	RV (km s^{-1})	*U* (km s^{-1})	*V* (km s^{-1})	*W* (km s^{-1})
2M0831+2042	− 35.8 ± 0.9	− 13.5 ± 0.5	34	38 ± 11	41 ± 12	10 ± 12	1 ± 12
2M0837+2050	− 39.2 ± 1.2	− 13.3 ± 0.6	37	30 ± 12	23 ± 10	2 ± 16	8.3 ± 8.3
2M0831+2244	59.7 ± 0.9	− 2.41 ± 0.59	21	4 ± 25	− 16 ± 19	12 ± 8.4	21 ± 13
TRAPPIST-1	924 ± 4[c]	− 467 ± 3[c]	60	−53[d]	−44[e]	−67[e]	16[e]

EPIC IDS AND OTHER PROPERTIES

	EPIC ID	Member	Age	parallax	period
2M0831+2042	212027121	Praesepe	∼700 Myr	5.36 ± 0.05 mas	0.556 ± 0.002 d
2M0837+2050	212035340	Praesepe	∼700 Myr	5.36 ± 0.05 mas	0.193 ± 0.000 d
2M0831+2244	212136544			13.5 ± 0.6 mas	0.292 ± 0.001 d
TRAPPIST-1	200164267		7.6 ± 2.2 Gyr[f]	82.4 ± 0.8[g] mas	3.29 ± 0.07 d

Notes:
(i) Spectral types are from West et al. (2011) and Liebert & Gizis (2006).
(ii) *J* and *K* magnitudes are from 2MASS Survey (Cutri et al. 2003).
(iii) *i* magnitudes are from Pan-STARRS Survey (Chambers et al. 2016).
(v) The distances and proper motions are from *Gaia* DR2 except for TRAPPIST-1.
References:
[a] Schmidt et al. (2015); [b]Gizis et al. (2000); [c]Theissen (2018); [d]Reiners et al. (2018); [e]Reiners & Basri (2009); [f]Burgasser & Mamajek (2017); [g]Van Grootel et al. (2018)

after 2M0837+2050), and 2MASS J08312608+2244586 (hereafter 2M0831+2244). In Section 2, we discuss the physical and photometric characteristics of the targets. In Section 3, we present the data reduction, flare photometry, and flare energy computation. We discuss the results in Section 4.

2 TARGET CHARACTERISTICS

The properties of our three targets are listed in Table 1. We have also listed the corresponding properties of TRAPPIST-1 in the same table to enable readers to compare its properties with other stars studied in this paper. We estimated radial velocities (RVs) and *UVW* components of space motion of our targets. The RVs were measured via cross-correlation of SDSS spectra to the Bochanski et al. (2007) template spectra, and the *UVW* were calculated from photometric distances and proper motions from SDSS-2MASS-WISE coordinates, described in Schmidt et al. (in preparation).

The stars 2M0831+2042 and 2M0837+2050 have spectral types of M7 and M8, respectively (West et al. 2011). Both objects are members of the open cluster Praesepe (Boudreault et al. 2012), which is also known as the Beehive Cluster, M44, or NGC 2632. Gaia Collaboration (2018b) estimate the distance of this cluster to be 186.2 pc (distance modulus = 6.350) and its age to be ∼700 Myr. The M7 and M8 stars mentioned above have Hα emission with equivalent width (hereafter EW) 9.3 ± 0.3 and 20.3 ± 0.6 Å, respectively (Schmidt et al. 2015).

2M0831+2244 is an M9 dwarf (West et al. 2011) located at a distance of 74.0 pc (Gaia Collaboration 2018a). It has an Hα emission with EW 7.3 ± 0.5 Å (Schmidt et al. 2015). It has a tangential velocity of ∼21 km s^{-1} suggesting that it is younger than another late-M dwarf TRAPPIST-1 which has a tangential velocity of ∼60 km s^{-1}. Youth is also supported by its rotation period of ∼7 h measured by *K*2. The BANYAN Σ tool (Gagné et al. 2018) suggests that it is not a member of any known nearby moving groups or stellar associations within 150 pc, by using astrometry measured by *Gaia* and the RV we estimated. So 2M0831+2244 is probably a field star.

3 DATA REDUCTION AND COMPUTATIONS

3.1 *K2* photometry

All three objects were observed by the *K*2 mission twice: once in Campaign 5 (27 April, 2015–10 July, 2015), and once in Campaign 18 (2018 May 12–July 2). Both observations were obtained in long cadence (∼30 min) mode (Jenkins et al. 2010). Additionally, 2M0831+2042 was observed in Campaign 16 (2017 December 7–2018 February 25). We performed point source function (psf) photometry to extract the light curves of our targets from their Target Pixel Files (TPFs). For this we also used the PYTHON package 'LIGHTKURVE' (Vinícius et al. 2018). The light curves were then detrended using the K2 Systematics Correction ('K2SC'; Aigrain, Parviainen & Pope 2016). The median count rates of 2M0831+2042, 2M0837+2050, and 2M0831+2244 are 192, 132, and 163 counts s^{-1}, respectively. The *Kepler* magnitude ($\tilde{K}_p$) of each object is listed in Table 1. $\tilde{K}_p$ was estimated using the Lund et al. (2015) relation $\tilde{K}_p \equiv 25.3–2.5$ log(count rate). We used only good quality ($Q = 0$) data points for flare photometry presented in this paper.

Using the Lomb–Scargle periodogram (hereafter LSP), we detected periodic features with periods of 0.556 ± 0.002, 0.193 ± 0.000, and 0.292 ± 0.001 d in the light curves of 2M0831+2042, 2M0837+2050, and 2M0831+2244, respectively. The uncertainties in the periods are based on half width at half-maximum (HWHM) of the periodogram peaks (Mighell & Plavchan 2013). These periods might be due to spot modulations of the objects: if so, the features most likely represent their rotation periods. If this is correct, the fastest rotator among our targets (2M0837+2050) rotates in a period which is shorter than 97 per cent of the M dwarfs which are classified as 'Class A rotators' by Newton et al. (2016). Interestingly, this target turns out to be the site of the largest flare we report in this paper. The phase folded light curves of three targets are shown in Figs 1, 2, and 3, respectively. The corresponding periodogram is also shown inside each figure.

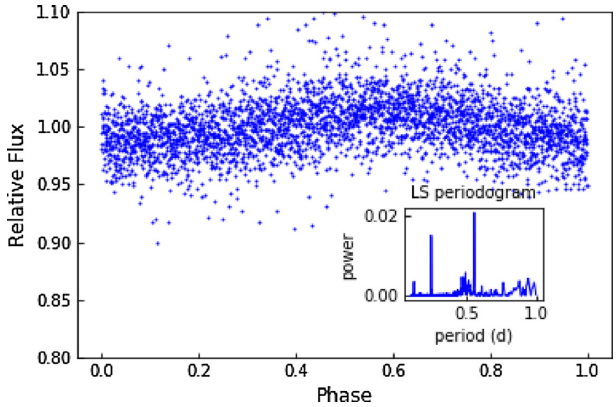

Figure 1. The phase folded *K*2 Campaign 5 light curve of M7 dwarf 2M0831+2042 corresponding to period of 0.556 d. The LSP is also shown inside. The second peak in the LSP corresponds to instrumental noise of ∼0.25 d.

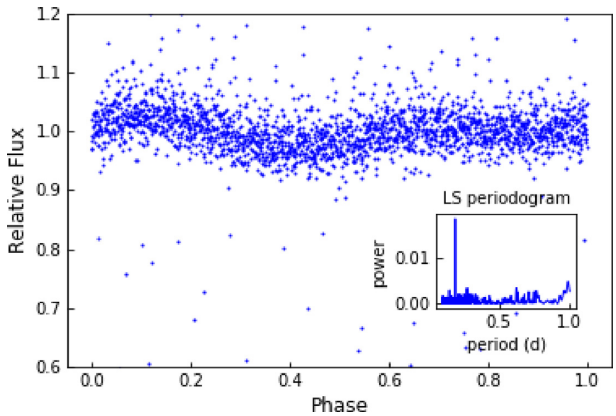

Figure 2. The phase folded *K*2 Campaign 18 light curve of M8 dwarf 2M0837+2050 corresponding to period of 0.193 d. The LSP is also shown inside.

3.2 Flare detection

We used the method described in Osten et al. (2012) to identify the flares in the light curves of our targets. For each data point in the *K2SC* detrended light curve, we calculated the relative flux $F_{\mathrm{rel},\,i}$, defined as

$$F_{\mathrm{rel},i} = \frac{F_i - F_{\mathrm{mean}}}{F_{\mathrm{mean}}}, \quad (1)$$

where F_{i} is the flux in *i*th epoch and F_{mean} is the mean flux of the entire light curve of each target. Using the values of $F_{\mathrm{rel},i}$, we then

Table 2. Properties of superflares.

Target	T_{peak} (BJD – 2454833)	$\Delta\tilde{K}_p$	ED (h)	Energy (erg)	Flare duration (d)
2M0831+2042	3444.1064	−3.2	13.7	1.3×10^{35}	0.74
2M0837+2050	3437.8544	−4.1	46.4	3.5×10^{35}	0.65
2M0837+2050	2378.0196	−1.1	1.7	1.3×10^{34}	0.06
2M0837+2050	2312.3112	−1.0	1.3	1.0×10^{34}	0.06
2M0837+2050	2377.7744	−1.1	1.0	7.4×10^{33}	0.04
2M0837+2050	2380.2058	−0.9	0.7	5.2×10^{33}	0.04
2M0831+2244	3457.9386	−4.4	50.21	6.1×10^{34}	0.40
2M0831+2244	3449.0100	−2.3	12.6	1.5×10^{34}	0.50
2M0831+2244	3426.7801	−1.3	1.6	1.9×10^{33}	0.06
2M0831+2244	3456.9579	−0.8	1.3	1.6×10^{33}	0.31
2M0831+2244	3440.8373	−1.1	1.2	1.4×10^{33}	0.08

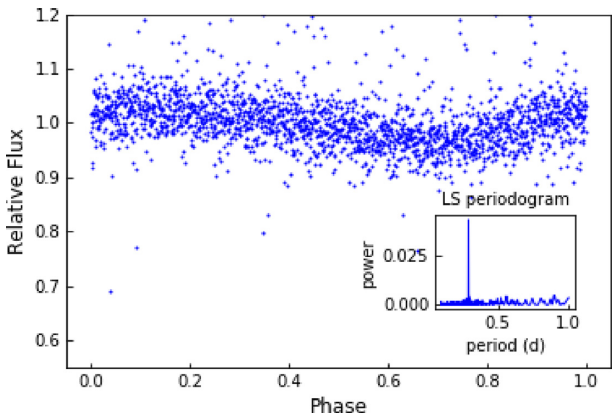

Figure 3. The phase folded *K*2 Campaign 18 light curve of M9 dwarf 2M0831+2244 corresponding to period of 0.292 d. The LSP is also shown inside.

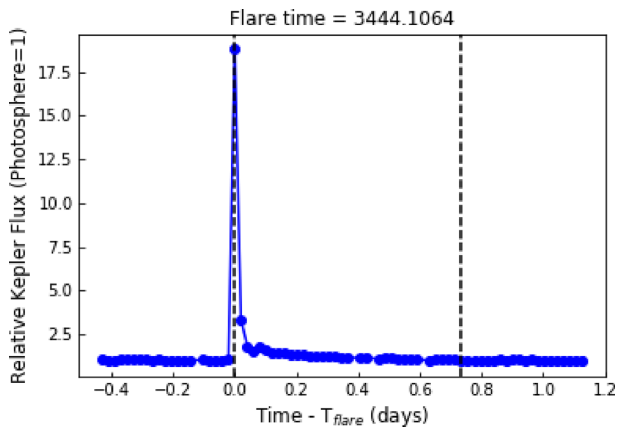

Figure 4. The superflare observed on M7 dwarf 2M0831+2042. The blue dots represent the observed data, and the vertical dashed lines represent the start and end times of the flare. The time along the *X*-axis is centred at the peak flare time which is mentioned on the top of the plot.

calculated a statistic ϕ_{ij} for each consecutive observation epoch (i, j) as

$$\phi_{ij} = \left(\frac{F_{\mathrm{rel},i}}{\sigma_i}\right) \times \left(\frac{F_{\mathrm{rel},j}}{\sigma_j}\right), \; j = i + 1. \quad (2)$$

Here σ_{i} is the error in the flux which is associated with the ith epoch. We then identified possible flare candidates in the light curve by using the false discovery rate analysis described in Miller et al. (2001). More detailed explanation regarding this method of flare detection can be found in Osten et al. (2012) and Paudel et al. (2018a). In order for the flare candidate to be qualified as a real flare event, we imposed an additional criterion, namely, that the detrended flux should exceed the photospheric level (the median count rate in the light curve) by 2.5σ. The final flare sample was chosen by inspecting the flare light curve and pixel level data by eye. We excluded flare candidates with only a single epoch brightening. All the flares identified on our targets have at least two epoch pairs for which $\phi_{ij} > 0$ and $F_{\mathrm{rel},\,i,\,j} > 0$ which ensures flux brightening for multiple times.

In the case of light curves measured in the long cadence mode, very small flares have relatively small amplitudes and last only for a few minutes (less than the duration of one long cadence at ∼30 min). They show up as single point brightening. Because of this, they do not qualify as flare candidates and hence are difficult to identify by using robust statistical techniques.

We searched for flares on our targets in all the available light curves using our flare detection method. We identified one strong superflare on 2M0831+2042, one on 2M0837+2050, and five superflares on 2M0831+2244 in Campaign 18 light curves. We also identified four superflares on 2M0837+2050 in Campaign 5 data. The peak flare times, equivalent durations, changes in *Kepler* magnitude ($\tilde{K}_p$) and flare durations of each superflares are listed in Table 2. We plot the strongest superflares on our targets in Figs 4, 5, and 6. Likewise, we plot the remaining superflares identified on 2M0831+2050 in Fig. 7 and those on 2M0831+2244 in Fig. 8, respectively. In each plot, the flare flux is normalized by the median flux in the corresponding light curve. The time on the top of each plot is the peak flare (*Kepler* mission) time of the corresponding flare inside the plot.

3.3 Flare energies

The most common method to estimate energy of a flare is to use its equivalent duration (ED) which is independent of the distance to the flaring object. It depends on the filter and the photospheric properties of the stars. It has units of time and is the area under the flare light curve (Gershberg 1972). It is the time during which the flare emits the same energy as the (sub)stellar object emits when it is in its quiescent state. We followed the procedures described in Gizis et al. (2017a,b) to estimate the flare energies.

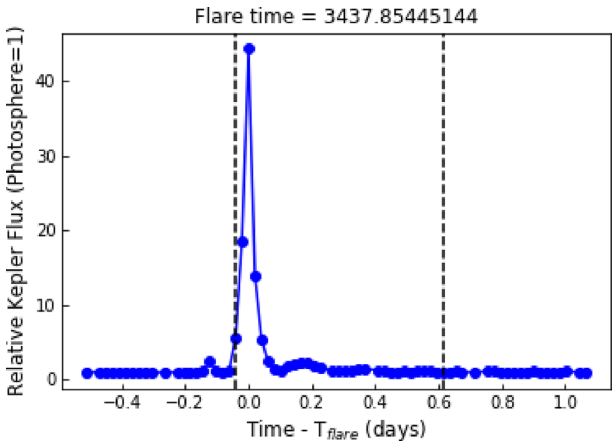

Figure 5. The largest superflare observed on M8 dwarf 2M0837+2050. The blue dots represent the observed data, and the vertical dashed lines represent the start and end times of the flare. The time along the *X*-axis is centred at the peak flare time which is mentioned on the top of the plot.

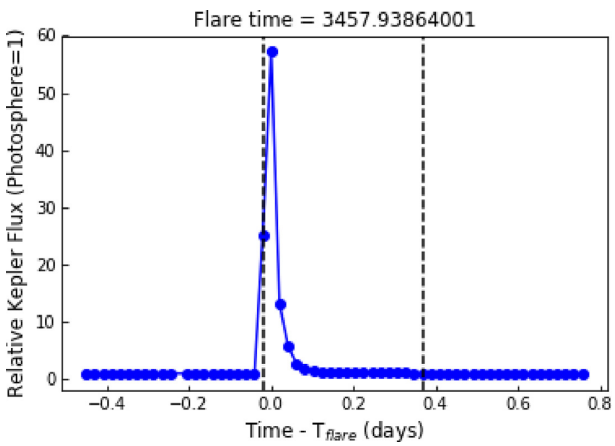

Figure 6. The largest superflare observed on M9 dwarf 2M0831+2244. The blue dots represent the observed data, and the vertical dashed lines represent the start and end times of the flare. The time along the *X*-axis is centred at the peak flare time which is mentioned on the top of the plot.

We first estimated the photospheric spectrum of our targets by using the matching active M dwarf template (Bochanski et al. 2007) normalized to match Pan-STARRS *i*-band photometry (Tonry et al. 2012; Chambers et al. 2016; Magnier et al. 2016). As a white light flare can be best described by using 10 000 K blackbody model (see e.g. Hawley & Pettersen 1991; Gizis et al. 2013), we modelled the flare as a 10 000 K blackbody normalized to have the same count rate through the *K*2 response curve as the photosphere of the corresponding object to estimate the energy emitted corresponding to an ED of 1 s. We emphasize that we calibrated the flare energies by extrapolating to ultraviolet and infrared wavelengths that are not detected by *K*2. So the energies reported here are those emitted by the blackbody continuum in UV/visible/IR wavelengths. They also include atomic emission features between 430 and 900 nm which can be detected by *K*2 but not the emission features in UV. The blackbody continuum dominates the flare energy budget in UV/visible wavelengths (Hawley & Pettersen 1991; Osten & Wolk 2015). We find that a flare with ED of 1 s on 2M0831+2042 has an energy of 2.6×10^{30} erg. Likewise, a flare with ED of 1s on 2M0837+2050 has 2.1×10^{30} erg and a flare with ED of 1 s on 2M0831+2244 has 3.4×10^{29} erg. We estimated the flare energies by multiplying these energies with the EDs of flares observed on corresponding targets. All the flare energies are listed in Table 2.

It should be noted that the flare duration of some large flares are longer than the rotational periods of the stars. In such cases, the estimated flare energies would be less than the real values if the flaring region is not located at polar region. The phase folded light curves shown in Figs 1, 2, and 3 however suggest that the rotational modulations lead to underestimation of the flare energies by very small fraction.

3.4 Comparison of flare rates with TRAPPIST-1

In Fig. 9, we compare the flare frequency distribution of TRAPPIST-1 with two of our targets: 2M0837+2050 and 2M0831+2244. This is a log–log plot of cumulative frequency($\tilde{\nu}$) of flare energies. The cumulative frequency of flares with energy E is the number of flares with energies $\geq E$. The flare energies of TRAPPIST-1 are taken from Paudel et al. (2018a). The total observation time of TRAPPIST-1 is 70.6 d and there are 39 flares with energies in the range (0.65–710) $\times 10^{30}$ erg in the UV/visible/IR wavelengths. The total observation times of 2M0837+2050 and 2M0831+2244 are 115.58 and 112.78 d, respectively, and include both Campaign 5 and 18.

The flare energy distribution of TRAPPIST-1 follows a power law of form

$$\log\tilde{\nu} = \alpha - \beta \log E \quad (3)$$

with $\beta \sim 0.6$ (Vida et al. 2017; Paudel et al. 2018a). In Fig. 9, in the case of TRAPPIST-1, the black solid line represents this distribution of observed flare energies while the dashed black line represents the extrapolation of the fitted line up to flare energy of 10^{35} erg to make it easier to compare with the other two targets. The extrapolation may not necessarily represent the true distribution. Likewise, the dashed lines overplotted on flare energies of 2M0837+2050 and 2M0831+2244 also represent the fitted lines. However, the lack of sufficient data point means they may not be the best representation of the real flare energy distribution of the corresponding targets. We should note here that TRAPPIST-1 light curves were obtained in short cadence (∼1 min) mode while we do not have such light curves for 2M0837+2050 and 2M0831+2244. This is why we did not detect flares of smaller energies that are detected in the TRAPPIST-1 light curve.

In Fig. 10, we compare the flare rates using the EDs of flares.

3.5 X-ray energy emitted during the largest flare on 2M0837+2050

To understand the relative impact of these superflares on exoplanets, we place these superflares in the solar context using the *GOES* (Geostationary Operational Environmental Satellite) flare classification scheme. The *GOES* flare classification scheme (A, B, C, M, X) is based solely on the peak 1−8 Å soft X-ray solar flux as observed from Earth, and each letter represents an increased order of magnitude from 10^{-8} to 10^{-3} W m^{-2} as observed at 1 au. In the units of energy emitted per second, *GOES* A1 flare corresponds to 2.8×10^{22} erg s^{-1} and *GOES* X1 flare corresponds to 2.8×10^{27} erg s^{-1}. To estimate the flare energy in the *GOES* bandpass, we use the results of Namekata et al. (2017) who compared the superflares of solar-type stars with the solar white light (WL) flares. They found a power-law relation between the WL flare energy ($E_{\rm WL}$, which is the

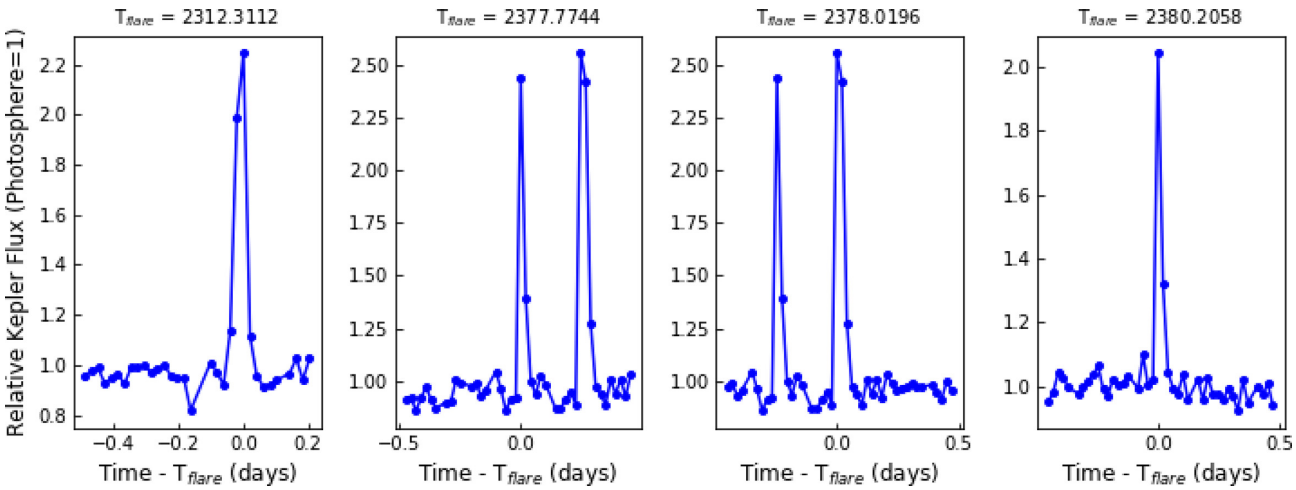

Figure 7. Other superflares observed on 2M0837+2050 in Campaign 5 data. The blue dots represent the observed data in each plot. The time along the *X*-axis is centred at the peak flare time which is mentioned on the top of each plot. Though the second and the third plots are similar, the only difference is the peak flare time mentioned on the top of them, corresponding to each flare.

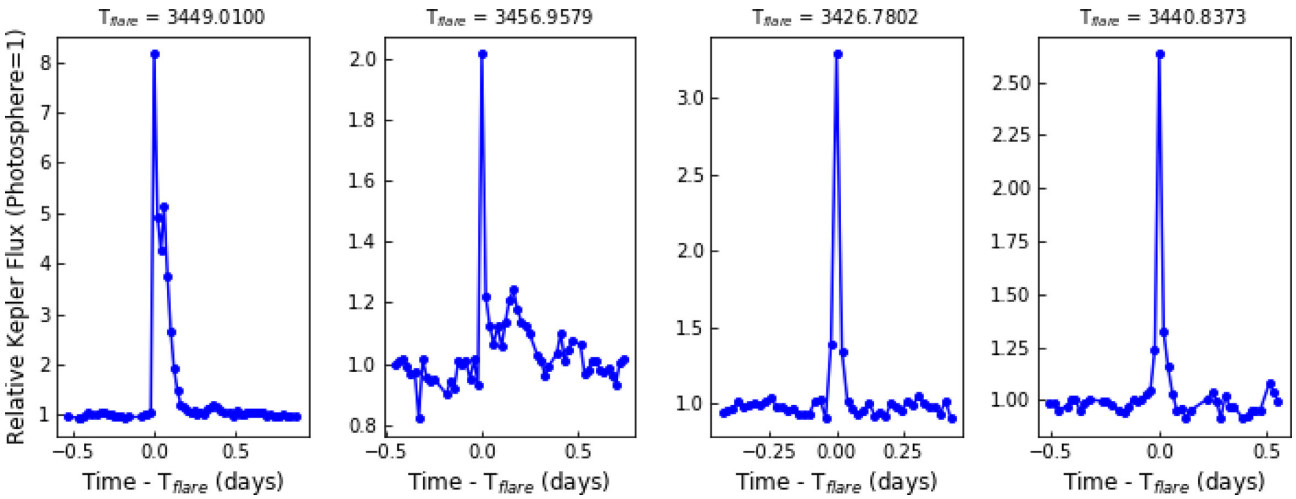

Figure 8. Other superflares observed on 2M0831+2244. The blue dots represent the observed data in each plot. The time along the *X*-axis is centred at the peak flare time which is mentioned on the top of each plot.

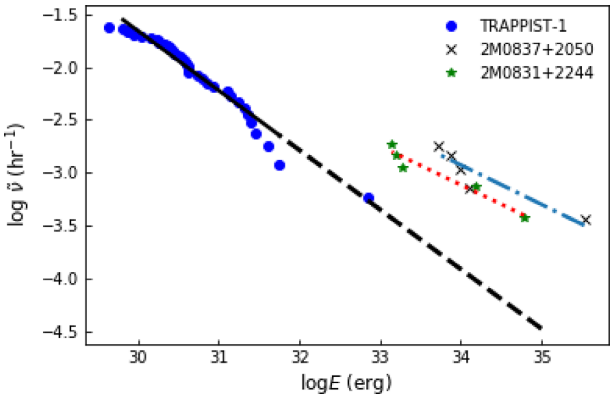

Figure 9. Comparison of flare frequency distribution of TRAPPIST-1 with 2M0837+2050 and 2M0831+2244. The solid black line plotted over TRAPPIST-1 flare energies is fitted line using parameters from Paudel et al. (2018a) and the dashed black line represents extrapolation to energy log E (erg) = 35.

same as the bolometric energy of the flare), and *GOES* soft X-ray (SXR) flux (F_{GOES}). Using fig. 5(b) in their paper, a 10^{30} erg WL flare corresponds to $\sim 6 \times 10^{-5}$ W m^{-2} in the *GOES* band. Using this relation, we estimate that $E_{\rm WL} = 1.67 \times 10^{34}\ F_{GOES}$, where the units of F_{GOES} are W m^{-2}. The estimated total WL flare energy of the largest superflare on 2M0837+2050 is 7.0×10^{35} erg.[1] Using the relation in Namekata et al. (2017), we get $F_{GOES} = 42$ W m^{-2} which is equivalent to 1.2×10^{32} erg s^{-1}, corresponding roughly to an X43 000 class flare. The X-ray flux in the HZ at 0.02 au (approximately the location of TRAPPIST-1 d) would be 1.1×10^5 W m^{-2} ($= 1.1 \times 10^8$ erg s^{-1} cm^{-2}). We caution the readers that the scaling based on solar-flares may not be necessarily same in the case of late-M dwarfs.

[1]We obtained this energy by first estimating the total energy in the *Kepler* band (E_{Kp}; 400–900 nm) and then converting E_{Kp} to bolometric energy by using the conversion relations in Osten & Wolk (2015) and Hawley et al. (2014).

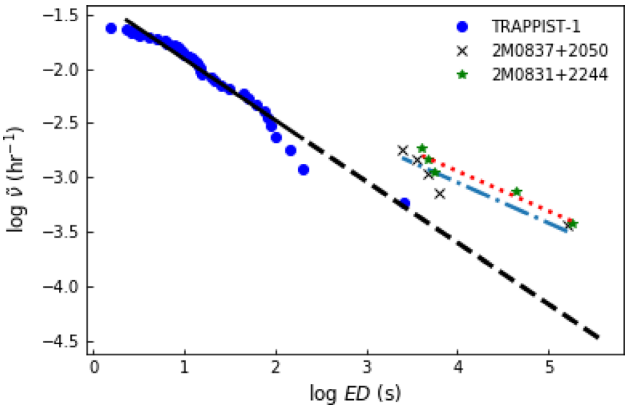

Figure 10. Same as Fig. 9. The flare energies are replaced by corresponding EDs.

4 SUMMARY AND DISCUSSION

We detected strong superflares on three late-M dwarfs: 2M0831+ 2042 (M7 V), 2M0837+2050 (M8 V), and 2M0831+ 2244 (M9 V), in *K2* long cadence light curves. The strong superflare observed on 2M0831+2042 has an ED of 13.7 h and has an estimated energy of 1.3×10^{35} erg. We detected five superflares on 2M0837+2050 with EDs in the range (0.7–46.4) h and estimated energies in the range (5.2–350) $\times$ 10^{33} erg. Likewise, we also detected five superflares on 2M0831+2244 with EDs in the range (1.2–50.21) h and estimated energies in the range (1.4–61) $\times$ 10^{33} erg.

2M0837+2050 and 2M0831+2244 now have the highest known superflare rates among late-M dwarfs. 2M0837+2050 is $\sim$ 700 Myr old and 2M0831+2244 also appears to be young as suggested by its tangential velocity estimate. In addition, they are rapidly rotating with periods of 0.193 $\pm$ 0.000 and 0.292 $\pm$ 0.001 d, respectively, which we detected in their *K*2 light curves using Lomb–Scargle periodogram. The high flare rates could be the result of strong magnetic dynamos enhanced by rapid rotation. Our results are in tension with those of Mondrik, Newton & Irwin (2019) who analysed the flare rates of a sample of 34 mid-to-late M dwarfs. They found that the flare rates are small among the slowest rotators with periods >70 d, but also are small among the fastest rotators with periods <10 d. Maximum flare rates are found among intermediate period rotators with periods of (10–70) d.

The rapid rotation rates and hence high flare rates of 2M0837+2050 and 2M0831+2244 could also be the result of their presence in binary systems. Douglas et al. (2017) measured the rotation periods of 677 low-mass stars ($1 \gtrsim M \gtrsim 0.1$ $M_\odot$) in the Praesepe cluster by using *K*2 light curves and found that $\sim$50 per cent of the rapidly rotating $\gtrsim$0.3 $M_\odot$ stars are in binary systems. The sample consisted of both confirmed and candidate binary systems but there is no information regarding binarity of the remaining $\gtrsim$0.3 $M_\odot$ fast rotators. Furthermore, Douglas et al. (2016) found that almost all $\gtrsim$0.3 $M_\odot$ fast rotating stars in the Hyades cluster, with age comparable to the Praesepe cluster, are in binary systems.

4.1 Flare rates of ∼700 Myr TRAPPIST-1 like objects

The flare rates of the M8 dwarf 2M0837+2050 are of particular importance for studies which are focused on the atmospheres of planets in the HZ of TRAPPIST-1. This is because both 2M0837+2050 and TRAPPIST-1 have a similar spectral type (M8) but different ages ($\sim$700 Myr, 7.6 Gyr respectively). We compare the flare frequency distributions of the two targets in Fig. 9. The energy of the largest flare on 2M0837+2050 is larger by 2.7 orders of magnitude than the largest flare observed on TRAPPIST-1 and occurs at approximately the same frequency. Our results may provide some guidance as to how large flares could have been on TRAPPIST-1 during its youth. While we do not have enough flares to reliably constrain the flare rates, the observed flares suggest that 10^{34} erg flares occur on 2M0837+2050 at a 10 times higher rate than on TRAPPIST-1. To be sure, the two M8 stars are not exactly comparable because 2M0837−2050 rotates almost 20 times faster than TRAPPIST-1. In view of this faster rotation, it is hardly surprising that the flare energy on 2M0837+2050 is hundreds of times larger than the largest flare on TRAPPIST-1.

The higher superflare rate of M9 dwarf 2M0831+2244 supports the claims we made in the previous paragraph. Comparison of the tangential velocity of TRAPPIST-1 ($\sim$60 km s^{-1}) with that of the 2M0831+2244 ($\sim$21 km s^{-1}) suggests that the latter is a younger object, with an age less than 7.5 Gyr. 2M0837+2050 and 2M0831+2244 have almost identical flare frequency distributions as seen in Fig. 9. The small differences between them might be due to differences in the rotation rates and/or the effective temperatures. The larger EW of Hα emission of 2M0837+2050 is also consistent with a higher flare rate than 2M0831+2244.

In Fig. 10, we compare the rates using only the EDs of flares. It suggests that the rates are almost similar for 2M0837+2050 and 2M0831+2244. However, we have only one data point of TRAPPIST-1 for which the ED value overlaps with the EDs of 2M0837+2050 and 2M0831+2244 flares. Though this single data point suggests that flares with comparable EDs occur more frequently on younger targets, we cannot perform any further statistical analysis and conclude anything at this point.

4.2 Particle flux associated with the largest superflare on 2M0837+2050

In Section 3.5, we estimated that the largest superflare from 2M0837+2050 is $\sim$X43 000 class in the *GOES* classification scheme of solar flares. For comparison, the Carrington event of 1859, probably the largest solar flare ever recorded, was $\sim$X45 class (Cliver & Dietrich 2013). Segura et al. (2010) estimate that the Great AD Leo flare (Hawley & Pettersen 1991) was X2300 class, and the extreme flare from young M dwarf binary DG CVn that triggered the Swift Burst Alert Telescope was estimated to be X600 000 class (Osten et al. 2016). Solar flares >X10 class have a $\sim$100 per cent probability of accompaniment by a CME (Yashiro et al. 2006), but events larger than the Carrington event have never been observed from the Sun and the relationship between CME properties and superflares is not yet known (e.g. Aarnio et al. 2011). To estimate the particle flux associated with the largest superflare on 2M0837+2050, we use the recently published results of Herbst et al. (2019) who combined the *GOES* data with the SphinX data and estimated a new power law for the peak size distribution of solar proton flux. The scaling relations of solar proton flux and soft X-ray flux are also derived by Cliver et al. (2012) and Takahashi, Mizuno & Shibata (2016). Herbst et al. (2019) found that the solar proton flux and F_{GOES} (W m^{-2}) are related as: $F(>10$ MeV in pfu$) = (1.22 \times 10^5\, F_{GOES} + 3.05 \exp(-0.001\, F_{GOES}))^{1.72}$. Extending this solar scaling relation out to observationally unconstrained superflare regime, we find that $F_{GOES} = 42$ W m^{-2} obtained in Section 3.5 leads to $F(>10\text{ MeV}) = 3.5 \times 10^{11}$ pfu at 1 au. This corresponds to a value of 8.7×10^{14} pfu at 0.02 au. For comparison, the >10 MeV

proton flux that Segura et al. (2010) estimated would have impacted a hypothetical HZ planet at 0.16 au for the Great AD Leo flare was 6×10^8 pfu, and this proton flux was sufficient to destroy 94 per cent of the O_3 column density of a modelled Earth-like planet.

In the case of some highly energetic SEP events (470 Mev to 4 GeV), the acceleration site of protons is CME driven shock which is located at 5–15 $R_\odot$ (Kahler 1994). Such distance is equivalent to ∼(0.002–0.007) au in the case of M8 dwarfs which have an average radii of ∼0.1 $R_\odot$, and is closer than the average orbital radii of HZ around them. This implies that it is possible for such protons to be injected out during the superflares on 2M0837+2050. However, this interpretation is solely based on the SEP events observed on the Sun. An anonymous referee has suggested that the average magnetic field strength of active M8 stars is much stronger than that of our Sun. Furthermore, the magnetic field topology of active M dwarfs might be different from that of our Sun (e.g. Donati & Landstreet 2009) and hence the acceleration site of the protons.

4.3 Estimation of CME masses associated with the superflares on 2M0837+2050

In studies of the Sun and active solar analogue stars, a strong correlation has been observed between the radiative energy emitted by a flare and the mass ejected in the associated CME. For example, Aarnio et al. (2011) showed that for the Sun, the flare energy emitted in X-rays correlates with CME mass in a power-law relationship. Aarnio, Matt & Stassun (2012) showed that the same solar relationship can be extended to extremely active, young solar-type stars, such that one relationship applies to X-ray flare energies spanning 10^{28} to 10^{38} erg, and the most energetic flares having associated CME masses of $\sim 10^{22}$ g (Aarnio et al. 2012). Osten & Wolk (2015) argued that this flare–CME relationship has a physical basis that is scalable and generally applicable to flaring stars from solar type down to mid-M type. Thus, it should be possible to apply empirically calibrated flare–CME relationships to the flares observed in our sample. The bolometric energies of superflares on 2M0837+2050 are in the range $\sim 1.0 \times 10^{34}$–$\sim 7.0 \times 10^{35}$ (see footnote in Section 3.5 for the estimation of bolometric energies), whereas the empirical relationship of Aarnio et al. (2012) applies to the X-ray emitted energy. However, as discussed by Günther et al. (2019), the empirical conversions between X-ray flare energies to bolometric flare energies (see e.g. Maehara et al. 2015) suggest that to good approximation one can adopt the relationship $E_{\rm bol} \approx 10^2 E_{\rm X\text{-}ray}$. Therefore, as in Günther et al. (2019), we modify the empirical relation of Aarnio et al. (2012) as $M_{\rm CME} = (2.7 \pm 1.2) \times (0.01 E_{\rm flare})^{0.63 \pm 0.04}$. where $E_{\rm flare}$ is the bolometric flare energy and all units are cgs. We infer CME masses associated with our observed flares to be in the range of $\sim 10^{20.6}$ to $\sim 10^{21.8}$ g.

4.4 Comparison of superflare on 2M0837+2050 with that on M2 dwarf GSC 8056−0482 for possible UV flux estimates

It is also instructive to compare the flare we discovered on one of our targets with a flare on another M dwarf, although they differ in their global properties. The superflare which we have discovered on the M8 dwarf 2M0837+2050 is larger by ∼100× than the $\sim 4 \times 10^{33}$ erg flare observed on GSC 8056−0482 by Loyd et al. (2018). The latter star (hereafter GSC) differs from our target star 2M0837+2050 in that it is warmer (sp. type = M2, $T_{\rm eff} \sim 3440$ K; Pecaut & Mamajek 2013) and younger (∼40 Myr; Kraus et al. 2014). In view of these differences, we need to exercise caution in making comparisons. The FUV energy of the superflare on GSC was estimated to be $10^{32.1}$ erg and is the largest energy flare ever observed in the FUV with the *Hubble Space Telescope (HST)*. Assuming the same ratio (18 per cent; Loyd et al. 2018) of FUV energy to bolometric energy of the GSC flare, we estimate that the FUV energy of our superflare on 2M0837+2050 is $>6.3 \times 10^{34}$ erg. This suggests that the FUV energy emitted during the superflare on 2M0837+2050 is greater than that on GSC by more than 2.7 orders of magnitude.

Loyd et al. (2018) analysed FUV flares on 12 M dwarfs in the ∼40 Myr Tuc-Hor young moving group, with spectral types M0.0–M2.3. They found that the flares on those M dwarfs were 100–1000× more energetic than those on field age (∼1–9 Gyr) M dwarfs. Combining their results with those we obtained in this paper, it is possible that strong flares with FUV energy in excess of 10^{36} erg can occur on the young ∼40 Myr M8 dwarfs. If superflares with energies of 10^{36} ergs occur frequently on young M8 dwarfs, the large amount of UV flux in the superflares may have serious consequences on the atmospheres of planets in HZ including complete loss of O_3 column (Segura et al. 2010; Tilley et al. 2017; Youngblood et al. 2017; Howard et al. 2018). Such results will be very important to study the environment around planet-hosting stars like TRAPPIST-1 when they were very young.

4.5 Time-scales of planet formation and life on Earth

The median lifetime of circumstellar discs, the planets forming regions, is ∼3 Myr and the dissipation rate is slower in case of low-mass stars than that of high-mass stars (Williams & Cieza 2011). The disc lifetimes of M dwarfs are of the order of ∼10 Myr. This is inferred from the fact that the dust disc around young M dwarfs are similar to those around T-Tauri stars whose disc life time-scales are ∼10 Myr (Boss 2006; Pascucci et al. 2011). On the other hand, the time-scale of formation of rocky planets in our Solar system is ∼10–120 Myr and that of gas giants is <5 Myr. A longer disc lifetime of M dwarfs may indicate a different time-scale of planet formation around them (Apai 2013). It is very likely the M dwarf planets might have already formed at ages of the Praesepe cluster.

On the other hand, the emergence of life also requires a minimum amount of time: in the only system for which we have data, it appears that an interval of some 200 Myr elapsed between the time of Earth formation and the time when the oldest known life emerged (Dodd et al. 2017). If this time-scale is relevant to emergence of life on exoplanets, then the level of flare activity on a star whose age is less than 200 Myr may not be relevant to astrobiology. The time-scale for decay in superflare rate may also set time-scale for life emergence. The latter also depends on planet properties such as the presence of magnetic fields.

4.6 How can the superflares be beneficial to studies regarding CMEs associated with stellar flares?

The presence of strong superflares highlights the importance of studying the distribution of magnetic field strengths on late-M dwarfs. Information about field strengths is necessary if we are to determine whether they are strong enough to supress the CMEs associated with the strong superflares. For example, Alvarado-Gómez et al. (2018) estimated that a large-scale dipolar field of strength 75 G is sufficient to supress the escape of the largest solar-like CMEs with kinetic energies of $\sim 3 \times 10^{32}$ erg. Assuming that the requisite field strength B to suppress a CME of a certain kinetic energy (KE) scales in such a way that $B^2/8\pi \sim$ KE, Mullan et al. (2018) have argued that a global stellar field of 750 G could suffice

to suppress CMEs in Trappist-1 with KE = 3×10^{34} ergs. Using the same scaling, magnetic fields of order 7.5 kG may be required to suppress CMEs with KE = 3×10^{36} ergs. Such suppression of energetic CMEs seems possible in some M dwarfs similar to WX UMa on which strong mean magnetic fields of strength 7.0 kG exist (Shulyak et al. 2017). But we do not know the upper limit of the flare energy and the KE of CMEs that can be emitted by an M dwarf of given mass and age. Hence it is important to the study of evolution of M dwarf flares through time to know the maximum flare energies that can be produced by each spectral type at different ages. In addition, we need more simultaneous observations of M dwarf flares at multiple wavelengths to constrain the flare energy distribution, which together with the maximum flare energies will enable us to estimate the total energy budgets received by the planets from their parent stars. Such energies will be valuable inputs to exoplanet atmosphere and climate models. If information can be obtained as to the time T which must elapse before life emerges on an exoplanet, then the results of atmosphere and climate models at times $>T$ could help put constraints on the habitability of planets in the HZ of M dwarfs.

4.7 Possible benefits of superflares to the planets in the HZ of M dwarfs

The superflares could also be beneficial to the planets in the HZ of M dwarfs. In an Earth-like planet orbiting within the classical HZ of a solar-type star or M dwarf, an H/He envelope having mass-fraction (ratio of mass of envelope to mass of core, $M_{\rm env}/M_{\rm core}$) of the order of 1 per cent may lead to very high surface temperatures and pressures unsuitable for the existence of liquid water. However, liquid water can be retained if the H/He envelope mass-fraction can be reduced to $\ll 10^{-3}$ via photoevaporation or other mechanisms (Owen & Mohanty 2016 and references therein). In this regard, the superflares may be helpful to strip off the thick H/He envelope if it is present. In addition, the superflares could help in producing haze forming monomers through photolysis of methane, in planets whose atmosphere is dominated by methane. The hazes might shield the planet's surface from UV radiation which in certain circumstances can be harmful to life to life (Tilley et al. 2017). Moreover, enhancement of photon fluxes is not always harmful to life. Certain UV photons can be beneficial for the onset of life by contributing to generation of the bases which occur in nucleic acids (Airapetian et al. 2016; Ranjan, Wordsworth & Sasselov 2017). And as another example of positive consequences of enhanced photon fluxes, we note that the optical photons which are enhanced during flares will increase the effectiveness of oxygenic photosynthesis in a planet lying in the HZ of a flare star (Mullan & Bais 2018).

ACKNOWLEDGEMENTS

The material in this paper is based upon work supported by the National Aeronautics and Space Administration (NASA) under award Nos. NNX15AV64G, NNX16AE55G and NNX16AJ22G. RRP acknowledges support from University of Delaware Dissertation Fellowship program. Some/all of the data presented in this paper were obtained from the Mikulski Archive for Space Telescopes (MAST). STScI is operated by the Association of Universities for Research in Astronomy, Inc., under NASA contract NAS5-26555. This paper includes data collected by the Kepler mission. Funding for the Kepler mission is provided by the NASA Science Mission directorate. This work has made use of data from the European Space Agency (ESA) mission *Gaia* (https://www.cosmos.esa.int/gaia), processed by the *Gaia* Data Processing and Analysis Consortium (DPAC, https://www.cosmos.esa.int/web/gaia/dpac/consortium). Funding for the DPAC has been provided by national institutions, in particular the institutions participating in the *Gaia* Multilateral Agreement. This research has made use of the VizieR catalogue access tool, CDS, Strasbourg, France. The original description of the VizieR service was published in A&AS 143, 23. This work made use of the http://gaia-kepler.fun crossmatch database created by Megan Bedell.

Softwares: PYTHON, IPython (Perez & Granger 2007), ASTROPY (Astropy Collaboration 2013), MATPLOTLIB (Hunter 2007), NUMPY (Oliphant 2015), LIGHTKURVE (Vinícius et al. 2018), K2SC (Aigrain et al. 2016), JUPYTER (Kluyver et al. 2016).

REFERENCES

Aarnio A. N., Stassun K. G., Hughes W. J., McGregor S. L., 2011, Sol. Phys., 268, 195
Aarnio A. N., Matt S. P., Stassun K. G., 2012, ApJ, 760, 9
Aigrain S., Parviainen H., Pope B., 2016, MNRAS, 459, 2408
Airapetian V. S., Glocer A., Gronoff G., Hébrard E., Danchi W., 2016, Nat. Geosci., 9, 452
Alvarado-Gómez J. D., Drake J. J., Cohen O., Moschou S. P., Garraffo C., 2018, ApJ, 862, 93
Apai D., 2013, Astron. Nachr., 334, 57
Astropy Collaboration, 2013, A&A, 558, A33
Barclay T., Pepper J., Quintana E. V., 2018, ApJS, 239, 2
Bochanski J. J., West A. A., Hawley S. L., Covey K. R., 2007, AJ, 133, 531
Boss A. P., 2006, ApJ, 643, 501
Boudreault S., Lodieu N., Deacon N. R., Hambly N. C., 2012, MNRAS, 426, 3419
Burgasser A. J., Mamajek E. E., 2017, ApJ, 845, 110
Chambers K. C. et al., 2016, preprint (arXiv:1612.05560)
Clements T. D., Henry T. J., Hosey A. D., Jao W.-C., Silverstein M. L., Winters J. G., Dieterich S. B., Riedel A. R., 2017, AJ, 154, 124
Cliver E. W., Dietrich W. F., 2013, J. Space Weather Space Clim., 3, A31
Cliver E. W., Ling A. G., Belov A., Yashiro S., 2012, ApJ, 756, L29
Crosley M. K., Osten R. A., 2018, ApJ, 862, 113
Cutri R. M. et al., 2003, 2MASS All Sky Catalog of point sources.
Davenport J. R. A., 2016, ApJ, 829, 23
Dodd M. S., Papineau D., Grenne T., Slack J. F., Rittner M., Pirajno F., O'Neil J., Little C. T. S., 2017, Nature, 543, 60
Donati J.-F., Landstreet J. D., 2009, ARA&A, 47, 333
Douglas S. T., Agüeros M. A., Covey K. R., Cargile P. A., Barclay T., Cody A., Howell S. B., Kopytova T., 2016, ApJ, 822, 47
Douglas S. T., Agüeros M. A., Covey K. R., Kraus A., 2017, ApJ, 842, 83
Dressing C. D., Charbonneau D., 2015, ApJ, 807, 45
Gagné J. et al., 2018, ApJ, 856, 23
Gaia Collaboration, 2018a, A&A, 616, A1
Gaia Collaboration, 2018b, A&A, 616, A10
Gershberg R. E., 1972, Ap&SS, 19, 75
Gillon M. et al., 2016, Nature, 533, 221
Gillon M. et al., 2017, Nature, 542, 456
Gizis J. E., Monet D. G., Reid I. N., Kirkpatrick J. D., Liebert J., Williams R. J., 2000, AJ, 120, 1085
Gizis J. E., Burgasser A. J., Berger E., Williams P. K. G., Vrba F. J., Cruz K. L., Metchev S., 2013, ApJ, 779, 172
Gizis J. E., Paudel R. R., Schmidt S. J., Williams P. K. G., Burgasser A. J., 2017a, ApJ, 838, 22
Gizis J. E., Paudel R. R., Mullan D., Schmidt S. J., Burgasser A. J., Williams P. K. G., 2017b, ApJ, 845, 33
Günther M. N. et al., 2019, preprint (arXiv:1901.00443)
Hawley S. L., Pettersen B. R., 1991, ApJ, 378, 725

Hawley S. L., Davenport J. R. A., Kowalski A. F., Wisniewski J. P., Hebb L., Deitrick R., Hilton E. J., 2014, ApJ, 797, 121
Herbst K., Papaioannou A., Banjac S., Heber B., 2019, A&A, 621, A67
Howard W. S. et al., 2018, ApJ, 860, L30
Howell S. B. et al., 2014, PASP, 126, 398
Hunter J. D., 2007, Comput. Sci. Eng., 9, 90
Jenkins J. M. et al., 2010, ApJ, 713, L120
Kahler S., 1994, ApJ, 428, 837
Kluyver T. et al., 2016, in Loizides F., Schmidt B., eds, Positioning and Power in Academic Publishing: Players, Agents and Agendas. IOS Press, Amsterdam, p. 87
Kraus A. L., Shkolnik E. L., Allers K. N., Liu M. C., 2014, AJ, 147, 146
Lacy C. H., Moffett T. J., Evans D. S., 1976, ApJS, 30, 85
Liebert J., Gizis J. E., 2006, PASP, 118, 659
Loyd R. O. P., Shkolnik E. L., Schneider A. C., Barman T. S., Meadows V. S., Pagano I., Peacock S., 2018, ApJ, 867, 70
Luger R. et al., 2017, Nat. Astron., 1, 0129
Lund M. N., Handberg R., Davies G. R., Chaplin W. J., Jones C. D., 2015, ApJ, 806, 30
Maehara H., Shibayama T., Notsu Y., Notsu S., Honda S., Nogami D., Shibata K., 2015, Earth Planets Space, 67, 59
Magnier E. A. et al., 2016, preprint (arXiv:1612.05242)
Mighell K. J., Plavchan P., 2013, AJ, 145, 148
Miller C. J. et al., 2001, AJ, 122, 3492
Mondrik N., Newton E., Irwin D. C. J., 2019, ApJ, 870, 10
Mullan D. J., Bais H. P., 2018, ApJ, 865, 101
Mullan D. J., MacDonald J., Dieterich S., Fausey H., 2018, ApJ, 869, 149
Namekata K. et al., 2017, ApJ, 851, 91
Newton E. R., Irwin J., Charbonneau D., Berta-Thompson Z. K., Dittmann J. A., West A. A., 2016, ApJ, 821, 93
Oliphant T. E., 2015, Guide to NumPy, 2nd edn. CreateSpace Independent Publishing Platform, USA
Osten R. A., Wolk S. J., 2015, ApJ, 809, 79
Osten R. A., Kowalski A., Sahu K., Hawley S. L., 2012, ApJ, 754, 4
Osten R. A. et al., 2016, ApJ, 832, 174
Owen J. E., Mohanty S., 2016, MNRAS, 459, 4088
Pascucci I. et al., 2011, in Johns-Krull C., Browning M. K., West A. A., eds, ASP Conf. Ser. Vol. 448, Planet Formation Around M-dwarf Stars: From Young Disks to Planets. Astron. Soc. Pac., San Francisco, p. 469
Paudel R. R., Gizis J. E., Mullan D. J., Schmidt S. J., Burgasser A. J., Williams P. K. G., Berger E., 2018a, ApJ, 858, 55
Paudel R. R., Gizis J. E., Mullan D. J., Schmidt S. J., Burgasser A. J., Williams P. K. G., Berger E., 2018b, ApJ, 861, 76
Pecaut M. J., Mamajek E. E., 2013, ApJS, 208, 9
Perez F., Granger B. E., 2007, Comput. Sci. Eng., 9, 21
Ranjan S., Wordsworth R., Sasselov D. D., 2017, ApJ, 843, 110
Reiners A., Basri G., 2009, ApJ, 705, 1416
Reiners A. et al., 2018, A&A, 612, A49
Ribas I. et al., 2016, A&A, 596, A111
Ricker G. R., 2014, J. Am. Assoc. Var. Star Obs., 42, 234
Schmidt S. J. et al., 2014, ApJ, 781, L24
Schmidt S. J., Hawley S. L., West A. A., Bochanski J. J., Davenport J. R. A., Ge J., Schneider D. P., 2015, AJ, 149, 158
Segura A., Walkowicz L. M., Meadows V., Kasting J., Hawley S., 2010, Astrobiology, 10, 751
Shulyak D., Reiners A., Engeln A., Malo L., Yadav R., Morin J., Kochukhov O., 2017, Nat. Astron., 1, 0184
Takahashi T., Mizuno Y., Shibata K., 2016, ApJ, 833, L8
Theissen C. A., 2018, ApJ, 862, 173
Tilley M. A., Segura A., Meadows V. S., Hawley S., Davenport J., 2017, preprint (arXiv:1711.08484)
Tonry J. L. et al., 2012, ApJ, 750, 99
Van Grootel V. et al., 2018, ApJ, 853, 30
Vida K., Kővári Z., Pál A., Oláh K., Kriskovics L., 2017, ApJ, 841, 124
Vinícius Z., Barentsen G., Hedges C., Gully-Santiago M., Cody A. M., 2018, KeplerGO/lightkurve.
West A. A. et al., 2011, AJ, 141, 97
Williams J. P., Cieza L. A., 2011, ARA&A, 49, 67
Yashiro S., Akiyama S., Gopalswamy N., Howard R. A., 2006, ApJ, 650, L143
Youngblood A. et al., 2017, ApJ, 843, 31

This paper has been typeset from a TEX/LATEX file prepared by the author.